PHYSICAL REVIEW B **110**, 235408 (2024)

Giant tunneling magnetoresistance and electroresistance in a two-dimensional VSi_2N_4/In_2Te_3 multiferroic tunnel junction

Shili Yang,[1] Zhifan Zheng,[1] Hua Hao,[2,*] Chun-Sheng Liu,[3] Xiaohong Zheng,[1,†] and Lei Zhang[4,5]
[1]*College of Information Science and Technology, Nanjing Forestry University, Nanjing 210037, China*
[2]*School of Physics, Hangzhou Normal University, Hangzhou 311121, China*
[3]*College of Electronic and Optical Engineering, Nanjing University of Posts and Telecommunications, Nanjing 210023, China*
[4]*State Key Laboratory of Quantum Optics and Quantum Optics Devices, Institute of Laser Spectroscopy, Shanxi University, Taiyuan 030006, China*
[5]*Collaborative Innovation Center of Extreme Optics, Shanxi University, Taiyuan 030006, China*

(Received 2 August 2024; revised 1 November 2024; accepted 25 November 2024; published 9 December 2024)

VSi_2N_4 is a newly reported magnetic semiconductor and is promising for being turned into a half metal. For this purpose, we construct a VSi_2N_4/In_2Te_3 van der Waals multiferroic heterostructure based on first-principles calculations. It is found that the inversion of ferroelectric polarization of monolayer In_2Te_3 can efficiently modulate the electronic states of monolayer VSi_2N_4. A phase transition of VSi_2N_4 from semiconductor to half metal can be effectually realized, leading to distinct electronic transport properties. Next, we design a magnetic tunnel junction (MTJ) (using the VSi_2N_4 monolayer as the tunneling barrier and the multiferroic heterostructure as the electrode) and investigate its transport properties in various magnetic configurations under different polarization directions of the ferroelectric In_2Te_3 layer by combining the nonequilibrium Green's function with density functional theory. The results show that the junction exhibits half-metallic transport in the parallel magnetic configuration and near-zero transport in the antiparallel magnetic configuration, resulting in a giant tunneling magnetoresistance ratio of $\sim 1 \times 10^{12}\%$. Moreover, a $\sim 1 \times 10^{17}\%$ tunneling electroresistance ratio is achieved in the parallel magnetic configuration accompanying the polarization reversal. The findings suggest that MTJs based on the VSi_2N_4/In_2Te_3 heterojunction have great potential for applications in multifunctional spintronic devices.

DOI: 10.1103/PhysRevB.110.235408

I. INTRODUCTION

Ferromagnetism, which is considered as a fundamental concept of condensed-matter physics, provides the basis for many magnetic storage and spintronic devices [1]. Since the first successful fabrication of graphene by Novoselov and Geim in 2004 [2], a large number of two-dimensional (2D) materials with extraordinary physical qualities and novel properties have been predicted and synthesized, attracting the attention of both theoretical and experimental researchers [3–7]. In particular, 2D ferromagnetic materials—which have atomic thickness, low energy consumption, fast device operation, and high storage density—are becoming more and more significant in a variety of semiconductor technologies and device applications. For nanoscale spintronic devices, atomically thin 2D ferromagnetic materials with the combination of large spin polarization and high Curie temperature (T_c) are of particular importance and interest [8,9]. Unfortunately, most of the 2D materials that have been predicted over a long period of time are nonmagnetic, which significantly limits their direct application in spintronics [10]. Great breakthroughs were made by Zhang's [11] and Xu's [12] teams, who observed bilayer $Cr_2Ge_2Te_6$ and monolayer CrI_3 exhibiting intrinsic ferromagnetism using polar magneto-optical Kerr effect microscopy in 2017. Since then, a variety of 2D materials with inherent magnetism has been discovered experimentally, including Fe_3GeTe_2, VSe_2, CoH_2, $NiPS_3$, and $CrBr_3$ [13–17]. Nevertheless, it remains extremely difficult to achieve significant 2D ultrahigh-density magnetic memory and nanodevices due to the low Curie temperature and weak ferromagnetic characteristics of existing 2D magnetic materials.

Currently, the research on 2D ferromagnetic materials focuses on two main directions. One is to search for new 2D ferromagnetic materials with high performance, such as robust ferromagnets with high Curie temperatures [18–20], wide spin-gap half metals [21,22], and high-mobility ferromagnetic semiconductors [23,24]. The other is to modulate known 2D ferromagnetic materials to achieve new properties or functions. Given this, the half metallicity of 2D ferromagnetic materials—that is, one spin channel being metallic and the other being insulating/semiconducting—has attracted an immense amount of interest due to 100% spin polarization [22,25–28]. However, the number of 2D intrinsic half-metallic materials, such as iron dihalide [22] and transition-metal (TM) dihydride [29], is very limited. Previous research has shown that external regulation, including chemical decoration [30,31], impurity doping [26,32], and transverse electric field [33,34], is responsible for the majority of the achieved half

---

[*] Contact author: hhao@hznu.edu.cn

[†] Contact author: xhzheng@njfu.edu.cn

metallicity. In addition, the construction of van der Waals heterojunctions also is one of the most important means of realizing half metallicity [35].

In this work, we focus on a recently reported 2D magnetic material VSi_2N_4, which belongs to the MA_2Z_4 family and is a ferromagnetic semiconducting material [36–38], with a broad range of applications in the fields of spintronics [39], environmental and energy applications [40,41], as well as catalysis and chemical reactions [42]. Since it has only one spin channel around the Fermi level, it is promising for being turned into a half metal by electron or hole doping. Using first-principles calculations, we build a van der Waals (vdW) multiferroic heterostructure to achieve half metallicity and control spin polarization of the VSi_2N_4 monolayer. The heterostructure is constructed by stacking a VSi_2N_4 monolayer atop a ferroelectric In_2Te_3 monolayer, which is selected for its intrinsic out-of-plane ferroelectric polarization and excellent lattice matching with the VSi_2N_4 monolayer. When VSi_2N_4 is in contact with In_2Te_3 in the $P_\downarrow$ state, the monolayer retains a ferromagnetic semiconductor; in contrast, the VSi_2N_4 monolayer transforms into a half metal when the polarization of the In_2Te_3 is reverted. Based on these results, we design a multiferroic tunnel junction (MTJ) in which the two electrodes can be set to have parallel and antiparallel magnetic moments and the polarization direction of the ferroelectric layer can be reverted, resulting in a giant tunneling magnetoresistance (TMR) and a giant tunneling electroresistance (TER).

II. COMPUTATIONAL DETAILS

The structural relaxations and electronic structure calculations of the heterostructure are performed using the Vienna *Ab initio* Simulation Package (VASP) [43,44], which is based on density functional theory (DFT) with the projector augmented wave method and a plane-wave basis set [45]. The generalized gradient approximation (GGA) in the form of Perdew-Burke-Ernzerhof (PBE) is adopted for the exchange-correlation potential [46]. The cutoff energy for the wave function is set to 520 eV. In the atomic structure relaxation, the vdW interaction is taken into account by the DFT-D3 method. The Brillouin zone (BZ) is sampled by a $9 \times 9 \times 1$ Monkhorst-Pack k-point mesh. Structural relaxations are performed with a value of 10^{-2} eV/Å for the residual force on each atom. The energy convergence criterion is set to 10^{-6} eV. Additionally, since the In_2Te_3 monolayers possess the quintuple-layer mirror asymmetric structure, the dipole correction needs to be enabled [47,48]. An effective U value of 3 eV is adopted on the d orbitals of the V atoms [36,49]. In order to minimize the interactions between the monolayer and its periodic images, a vacuum spacing of 15 Å is used for all calculations.

The calculations of quantum transport are performed using the ATOMISTIX TOOLKIT (ATK) package [50] based on the DFT combined with the nonequilibrium Green's function (NEGF) technique [51]. In the transport computations, the first BZ of the electrodes is sampled by a k-point grid of $9 \times 1 \times 72$ for self-consistency and by $61 \times 1 \times 72$ for transmission calculations, with a density mesh cutoff of 95 Hartree for the real-space grid.

The spin polarization in parallel configuration (PC) and in antiparallel configuration (APC) is defined as

$$\mathrm{SP}_{\mathrm{PC/APC}} = \frac{T^{\uparrow}_{\mathrm{PC/APC}} - T^{\downarrow}_{\mathrm{PC/APC}}}{T^{\uparrow}_{\mathrm{PC/APC}} + T^{\uparrow}_{\mathrm{PC/APC}}} \times 100\%, \tag{1}$$

where $T_\uparrow$ and $T_\downarrow$ represent the spin-up and spin-down transmission coefficients of the MTJ under various magnetic configurations. Then, the corresponding tunneling magnetoresistance ratio is defined as

$$\mathrm{TMR} = \frac{|T_{\mathrm{PC}} - T_{\mathrm{APC}}|}{\min(T_{\mathrm{PC}}, T_{\mathrm{APC}})} \times 100\%, \tag{2}$$

where T_{PC} and T_{APC} indicate the transmission coefficients of MTJs for different magnetic configurations, respectively. At last, the tunneling electroresistance ratio is calculated by

$$\mathrm{TER} = \frac{|T_{\mathrm{up}} - T_{\mathrm{dn}}|}{\min(T_{\mathrm{up}}, T_{\mathrm{dn}})} \times 100\%, \tag{3}$$

where T_{up} and T_{dn} represent the transmission coefficients of the MTJs at the Fermi level for In_2Te_3 with $P_\uparrow$ and $P_\downarrow$ polarizations, respectively.

III. RESULTS AND DISCUSSION

All 2D ferroelectric materials with out-of-plane polarization are possible candidates for tuning VSi_2N_4 to achieve two distinct magnetic states. A proper candidate must at first satisfy the lattice-matching requirement, namely, the lattice constant of the obtained supercell should be as small as possible to decrease the computational burden. After extensive comparison and screening, it is found that In_2Te_3 will be the best in this aspect since the supercell of the vdW heterostructure constructed with these two materials will be the smallest. Thus, In_2Te_3 is chosen as the candidate for this study. The optimized lattice constants of the monolayer VSi_2N_4 and monolayer In_2Te_3 are 2.88 Å and 4.40 Å, respectively, which is consistent with previous theoretical results [52,53]. To build the supercell of the van der Waals (vdW) heterostructure, we choose $\sqrt{7} \times \sqrt{7}$ VSi_2N_4 unit cells and $\sqrt{3} \times \sqrt{3}$ In_2Te_3 unit cells, with initial lattice constants of the supercell as 7.620 Å and 7.621 Å, respectively. In this way, the initial lattice mismatch between the supercells of the two materials is only about 0.026%. In the structural relaxation, we consider four configurations of the VSi_2N_4/In_2Te_3 heterostructure with high symmetry in the In_2Te_3 $P_\uparrow$ case; namely, configuration A1 in which the Si atoms of the VSi_2N_4 layer are located right above the top Te atom of the In_2Te_3 layer, configuration A2 in which the N atoms of the VSi_2N_4 layer are located above the top Te atoms of the In_2Te_3 layer, configuration A3 in which the Te atom of the In_2Te_3 layer is located exactly beneath the midpoint between the two N atoms of the VSi_2N_4 layer, and configuration A4 in which the V atoms of the VSi_2N_4 layer are located above the top Te atoms of the In_2Te_3 layer [see Figs. 1(a)–1(d)]. Based on first-principles calculations, the calculated total energies E and the optimal interlayer distances d of the four configurations under different polarization states are listed in Table I. It is seen that the total energy difference of each configuration under the same polarization is very small, and configuration A4 is the most stable. Eventually, we

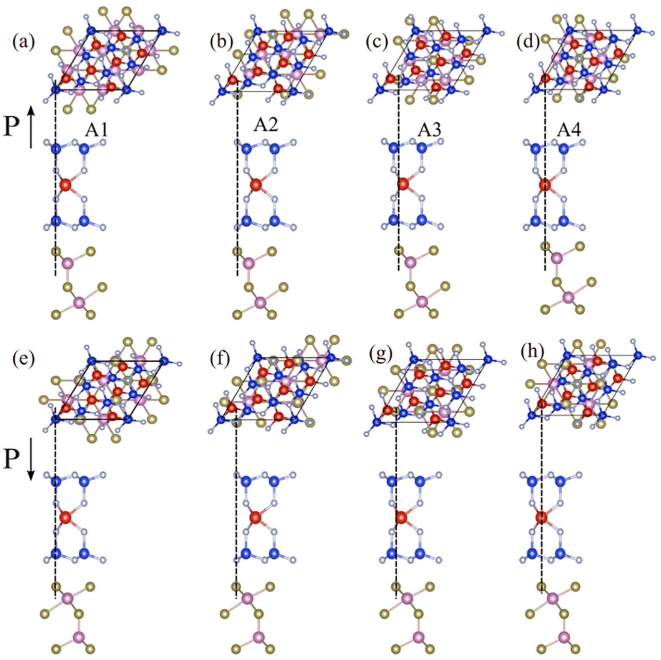

FIG. 1. (a)–(h) VSi_2N_4/In_2Te_3 multiferroic heterostructures with various stacking configurations under different polarization states. The (a)–(d) $P_\uparrow$ and (e)–(h) $P_\downarrow$ states for stacking configurations A1, A2, A3, and A4 are displayed. The red, blue, gray, purple, and yellow balls represent the V, Si, N, In, and Te atoms, respectively.

select the fully optimized configuration A4 to further study its electronic properties and construct the MTJ.

The monolayer VSi_2N_4 is a compound of a septuple-layer six-membered ring (SMR) material, and its structure is similar to the experimentally synthesized $MoSi_2N_4$ family [52]. According to previous reports, VSi_2N_4 is ferromagnetic with T_c as high as 500 K [38,54]. If the MTJs based on VSi_2N_4 layers have a large TMR, they are promising for practical applications because of their high T_c and environmental stability. For the monolayer electronic properties, Figs. 2(a) and 2(b) show the band structures of the freestanding In_2Te_3 monolayer and VSi_2N_4 monolayer, respectively. It is evident that the VSi_2N_4 monolayer is a semiconductor, with both its conduction band minimum (CBM) and valence band maximum (VBM) originating from the spin-up channel (often known as a half semiconductor). With a band gap of 0.62 eV, the ferroelectric In_2Te_3 monolayer also exhibits semiconductor characteristics. Additionally, In_2Te_3 shows a considerable out-of-plane polarization of 0.74 $\mu C/cm^2$, and the intrinsic dipole induces an electrostatic potential difference of 0.88 eV across its two surfaces, as shown in Fig. 2(c). Consequently, In_2Te_3 has two ferroelectric states that are dynamically stable, with the polarized states designated as $P_\uparrow$ or $P_\downarrow$. These two states can be switched from one to the other by an external electric field. More importantly, the In_2Te_3 monolayer retains its current state even when the external electric field is removed, known as nonvolatility.

TABLE I. Total energies (E) and interlayer distances (d) of different stacking configurations of the VSi_2N_4/In_2Te_3 heterostructure.

	VSi_2N_4/In_2Te_3 ↑		VSi_2N_4/In_2Te_3 ↓	
Configuration	E (eV)	d (Å)	E (eV)	d (Å)
A1	−452.4795	3.396	−452.4219	3.428
A2	−452.4808	3.401	−452.4220	3.433
A3	−452.4791	3.407	−452.4193	3.443
A4	−452.4815	3.394	−452.4221	3.436

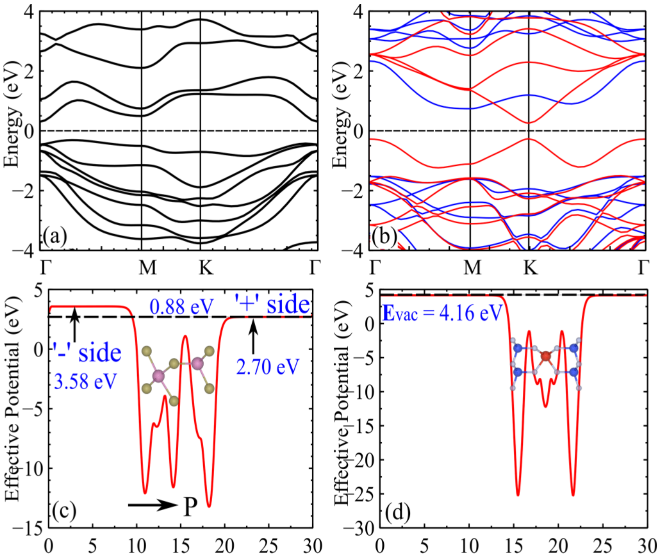

FIG. 2. Band structure of (a) monolayer In_2Te_3 and (b) monolayer VSi_2N_4, and the effective potential of (c) In_2Te_3 and (d) VSi_2N_4 along the direction of the vacuum layer, with 0.88 eV indicating the potential difference between the two surfaces. The Fermi level is set to zero. The two sides of In_2Te_3 are represented by the "−" side and "+" in (c).

Next, we discuss how the polarization of In_2Te_3 affects the electrical properties of VSi_2N_4. In traditional ferroelectric tunnel junctions, a large voltage or electric field is usually used to revert the polarization direction, and a small voltage is used to read the resistance state of the tunnel junction. In this work, it is assumed that the reversion of the polarization directions is induced by a vertical electrical field, which will drive the Te atoms in the internal Te layer from right above the lower In-layer atoms to right below the upper In-layer atoms, leading to the movement of the negative-charge center. As shown in Figs. 3(a)–3(d), the spin-down and spin-up projected bands of the In_2Te_3 layer are almost degenerate in energy, whereas the VSi_2N_4 layer still shows strong spin polarization in its bands. Figures 3(a) and 3(b) show that in the $P_\uparrow$ polarization state, the spin-down energy bands of VSi_2N_4 do not reach the Fermi level, whereas the spin-up energy bands do. Compared to the freestanding VSi_2N_4 monolayer, the spin-up electronic states arising from the VSi_2N_4 layer in the VSi_2N_4/In_2Te_3 $P_\uparrow$ case are energetically downshifted and cross the Fermi level. As a result, the VSi_2N_4 layer exhibits half-metallic properties in the VSi_2N_4/In_2Te_3 $P_\uparrow$ state. In the VSi_2N_4/In_2Te_3 $P_\downarrow$ state, the electronic structure of the heterostructure maintains a common band gap and demonstrates semiconductor behavior. In contrast to the VSi_2N_4/In_2Te_3 $P_\uparrow$ state, the spin-up electronic states originating from the VSi_2N_4 layer shift upward in energy and no longer traverse the Fermi level, while

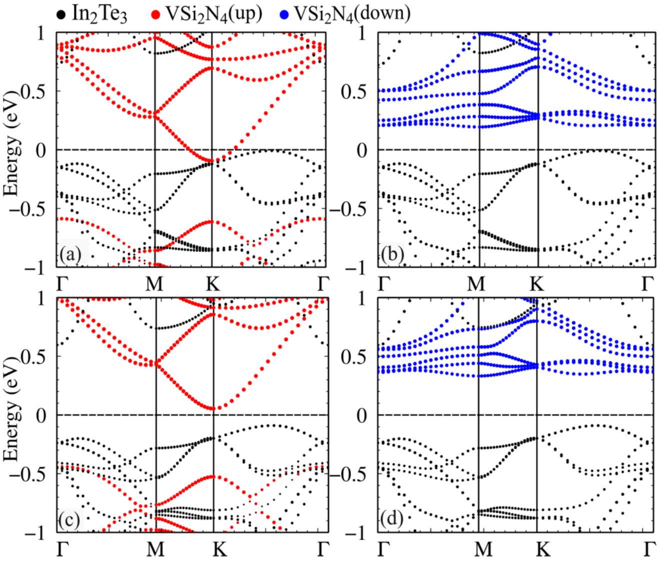

FIG. 3. Spin-resolved and layer-projected band structure of VSi$_2$N$_4$/In$_2$Te$_3$ multiferroic heterostructure with In$_2$Te$_3$ in (a), (b) $P_\uparrow$ and (c), (d) $P_\downarrow$ polarizations. The Fermi level is set to zero. The energy bands of (a), (c) spin-up electrons and (b), (d) spin-down electrons are shown.

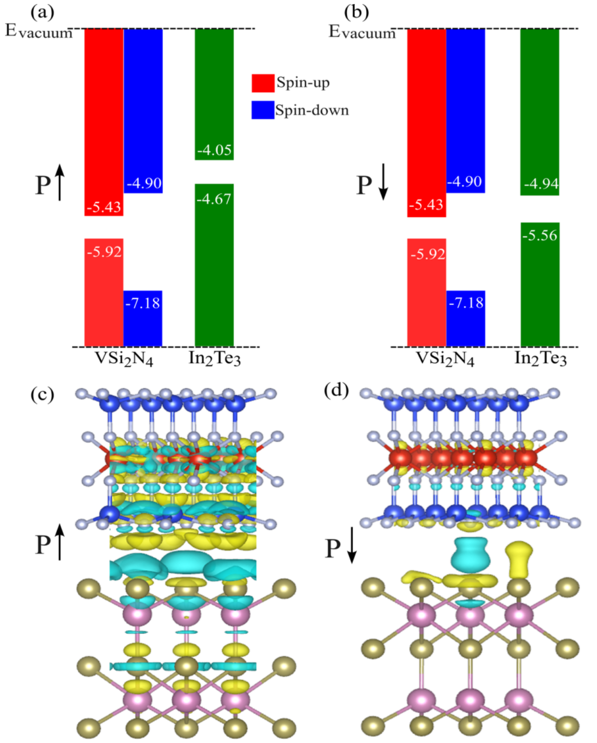

FIG. 4. Band alignments of monolayer VSi$_2$N$_4$ and monolayer In$_2$Te$_3$ in the (a) $P_\uparrow$ and (b) $P_\downarrow$ polarization states; and the three-dimensional isosurface of the differential charge density of the multiferroic heterostructures with (c) $P_\uparrow$ and (d) $P_\downarrow$ states, where the blue and yellow regions, respectively, indicate electron depletion and accumulation. The energy values are shown in eV units.

the electronic states from In$_2$Te$_3$ shift slightly downward and away from the Fermi level. In summary, when the $P_\uparrow$ state in the VSi$_2$N$_4$/In$_2$Te$_3$ heterostructure shifts to the $P_\downarrow$ state, the VSi$_2$N$_4$ transits from a half metal to a semiconductor.

When the ferroelectric polarization switches between the $P_\uparrow$ and $P_\downarrow$ states, there is a difference in charge transfer at the interfaces of the VSi$_2$N$_4$ and In$_2$Te$_3$ contacts, which accounts for the observed phase transformation behavior and can be clearly seen from the band structure shown in Fig. 3. Generally, whether or not charge transfer between two materials occurs depends on the contact potential difference due to their different work functions. It is well known that due to the built-in electrical field induced by the out-of-plane polarization, the ferroelectric material In$_2$Te$_3$ has two distinct vacuum energy levels on its two surfaces, leading to two different work functions [55]. Since the polarization direction points from the negative (−) charge to the positive (+) charge, for convenience, we may call these two surfaces as the "−" side and "+" side, respectively. To explain the different charge transfer in the two polarization states, the work functions of VSi$_2$N$_4$ and In$_2$Te$_3$ are calculated, and the initial band alignments before contact are further obtained based on these work functions [Figs. 4(a) and 4(b)]. Previous research indicates that when materials with different work functions come into contact, electrons migrate from one side of a material with the lower work function to the one with the higher work function until their Fermi levels are equal [56]. In other words, charge transfer between two stacked materials occurs only when the VBM of one material is higher than the CBM of the other, owing to the relative shift in their energy bands [57–59]. In the $P_\uparrow$ state, the spin-up and spin-down CBM of VSi$_2$N$_4$ is lower than the VBM of In$_2$Te$_3$ [see Fig. 4(a)], which belongs to the type-III band alignment and will lead to charge transfer between the two interfaces. Since the spin-up CBM is lower than the spin-down CBM, electrons in In$_2$Te$_3$ predominantly migrate to the spin-up CBM of VSi$_2$N$_4$, leaving the spin-down CBM largely unoccupied. This transfer results in the spin-up CBM crossing the Fermi level, whereas the position of the spin-down CBM remains relatively unchanged. Hence, the VSi$_2$N$_4$ layer exhibits half-metallic properties. On the contrary, both the spin-up and spin-down CBM (VBM) of VSi$_2$N$_4$ are higher (lower) than the VBM of In$_2$Te$_3$ in the $P_\downarrow$ state, suggesting a type-II band alignment and that the charge transfer is almost nonexistent between the two interfaces. Therefore, the VSi$_2$N$_4$ layer presents semiconductor characteristics in the VSi$_2$N$_4$/In$_2$Te$_3$ $P_\downarrow$ state. We also compute the differential charge density, as shown in Figs. 4(c) and 4(d), to better visualize the charge transfer. It is evident that there is hardly any electron or hole aggregation in the $P_\downarrow$ configuration, whereas there is a significant amount of electron (hole) aggregation surrounding VSi$_2$N$_4$(In$_2$Te$_3$) in the $P_\uparrow$ configuration.

Based on these findings, we design a MTJ that consists of a vertical VSi$_2$N$_4$/In$_2$Te$_3$ heterostructure as the left and right electrodes and a VSi$_2$N$_4$ layer as the central barrier, as shown in Fig. 5. The rectangular electrode supercell size is 7.62 × 13.20 Å along the x and z directions. The length of the central region is 39.6 Å, with the length of the In$_2$Te$_3$ gap region as 7.62 Å. The magnetic configuration of the VSi$_2$N$_4$ layers of the heterojunction electrodes is set to be parallel or antiparallel under two different polarization states to further explore the MTJ characterization. Next, we investigate the transport properties by calculating the transmission spectra of

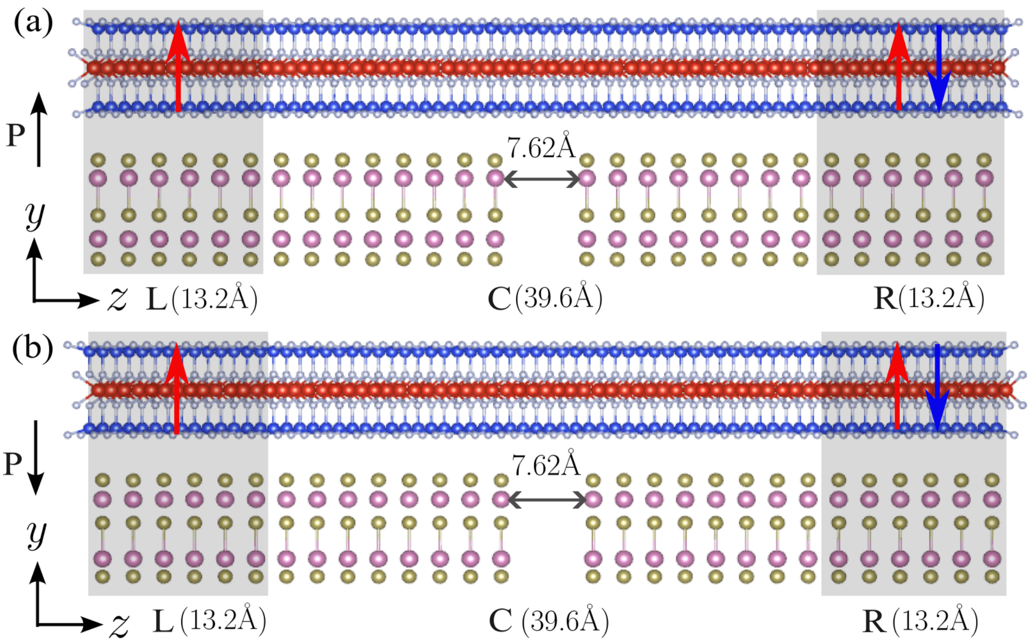

FIG. 5. The MTJ structures in (a) the $P_\uparrow$ state and (b) the $P_\downarrow$ state. The structure consists of three parts: the left (L) and right (R) electrodes, and the central scattering region (C). The left and right electrodes are VSi$_2$N$_4$/In$_2$Te$_3$ vdW multiferroic heterojunctions, and the central channel region is a VSi$_2$N$_4$ monolayer. The shadowed area marks the electrode supercell. The red and blue vertical arrows indicate the possible magnetization directions. The numbers indicate the lengths of different parts in the junction.

MTJ at zero bias, which are presented in Figs. 6(a)–6(c). It is evident that in the configuration of parallel magnetization ($M_{\uparrow\uparrow}$) of VSi$_2$N$_4$ and polarization up ($P_\uparrow$) state of In$_2$Te$_3$ (abbreviated as $P_\uparrow$-$M_{\uparrow\uparrow}$), the transmission around the Fermi

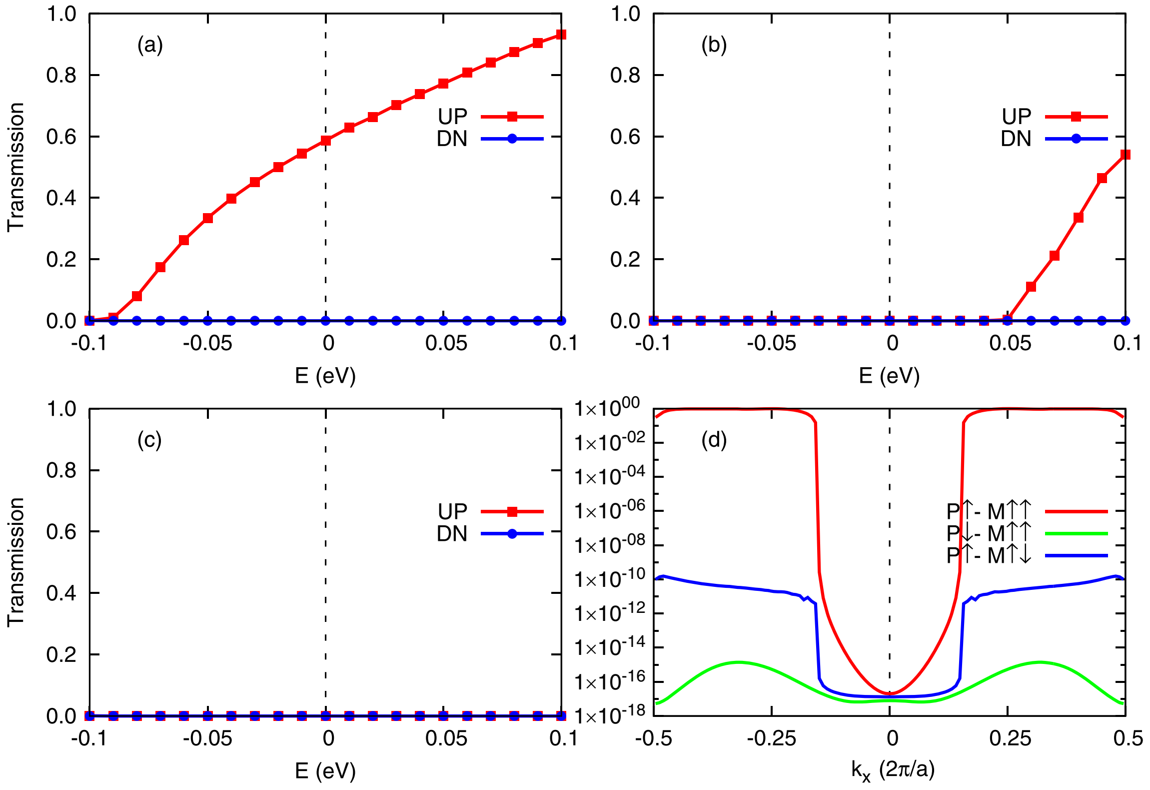

FIG. 6. Transmission spectra of the MTJ for different polarization and magnetization configurations: (a) $P_\uparrow$-$M_{\uparrow\uparrow}$, (b) $P_\uparrow$-$M_{\uparrow\downarrow}$, and (c) $P_\downarrow$-$M_{\uparrow\uparrow}$. The spin-up and spin-down transmissions are represented by red and blue lines, respectively. (d) The k_x-resolved transmission of the spin-up channel at the Fermi level.

level is mainly contributed by the spin-up channel, whereas the transmission in the spin-down channel is almost completely suppressed, and thus half-metallic transport is achieved [see Fig. 6(a)]. Obviously, due to the vacuum gap between the In_2Te_3 in the two leads, the Bloch states of In_2Te_3 coming from deep in the leads are all blocked, and the transmission around the Fermi level is contributed by the spin-up band of VSi_2N_4 crossing the Fermi level. In the case of the $P_\uparrow$-$M_{\uparrow\downarrow}$ configuration, the spin-up channel mostly contributes to the transmission at 0.05 eV above the Fermi level, while there is no transmission at the Fermi level [Fig. 6(b)]. In the case of $P_\downarrow$-$M_{\uparrow\uparrow}$, both spin channels are blocked in a large energy range around the Fermi level [Fig. 6(c)]. The above results are quite consistent with the features exhibited in the spin-resolved and layer-projected band structures (Fig. 3).

It is well known that the transport properties of either a material or a device depend on the behavior near the Fermi level. Under low bias, the system is in the linear response regime and the current will be proportional to the transmission function at the Fermi level. Thus, it is reasonable to calculate the TMR and TER ratios by the transmission function value at the Fermi level [60,61]. According to the calculated transmission coefficients at the Fermi level (namely, $T_\uparrow = 0.587$ and $T_\downarrow = 2.25 \times 10^{-17}$ in the $P_\uparrow$-$M_{\uparrow\uparrow}$ case [see Fig. 6(a)]; $T_\uparrow = 3.01 \times 10^{-11}$ and $T_\downarrow = 3.29 \times 10^{-12}$ in the $P_\uparrow$-$M_{\uparrow\downarrow}$ case [see Fig. 6(b)]; and $T_\uparrow = 3.40 \times 10^{-16}$ and $T_\downarrow = 4.07 \times 10^{-18}$ in the $P_\downarrow$-$M_{\uparrow\uparrow}$ case [see Fig. 6(c)]), after calculations with Eqs. (1)–(3), this MTJ achieves nearly 100% spin polarization in the $P_\uparrow$-$M_{\uparrow\uparrow}$ case, a TMR ratio of up to $1.93 \times 10^{12}\%$, and a TER ratio of up to $1.72 \times 10^{17}\%$. The high or low conductance in the $P_\uparrow$ or $P_\downarrow$ cases is obviously a result from the band structures, as seen from Fig. 3. At the same time, the orbital hybridization revealed in the differential charge density also plays its role. In the $P_\uparrow$ case, strong orbital hybridization between the two materials at the interface will be beneficial for the electron transfer and partly responsible for the large equilibrium conductance in this case. On the contrary, in the $P_\downarrow$ case, there is negligible charge accumulation at the interface, indicating weak orbital hybridization between the two materials, which is not beneficial for electron transfer and partly responsible for the low conductance.

To have deeper insight into the transport properties, the $k_{//}$-resolved transmission functions have been studied, with the spin-up channel contributions of the equilibrium transmission coefficients presented in Fig. 6(d) (spin-down channel not shown due to its negligible contribution in all cases). Since y is along the vacuum direction, with only one k point taken in this direction, the $k_{//}$ is only along the x direction and the $k_{//}$-resolved transmission for certain energy is a one-dimensional function. It is found that under the $P_\uparrow$-$M_{\uparrow\uparrow}$ configuration, the k points in the $0.35\frac{2\pi}{a}$ range around the boundary point $\pm\frac{\pi}{a}$ of the first Brillouin zone contribute the most, and the transmission is even close to 1. However, in the range $[-0.15, 0.15]\frac{2\pi}{a}$ around the Γ point, we observe a transmission gap. Actually, this happens to all three cases. In the polarization up case, if we revert the magnetization of the right lead, namely, in the $P_\uparrow$-$M_{\uparrow\downarrow}$ case, due to spin mismatch, the spin-up channel in the VSi_2N_4 layer is completely blocked. In this case, the transmission is only mediated by In_2Te_3. However, due to the real-space gap, the transmission is negligibly small, with the magnitude of 10^{-11}. Further, under the parallel magnetization configuration ($M_{\uparrow\uparrow}$), if we revert the polarization, the transmission will become even smaller since, for both spin-up and spin-down channels, both VSi_2N_4 and In_2Te_3 are insulating. Note that the spin phenomena at the interface, such as spin transparency of the interface, spin back flow, and interface-induced spin localization that could induce effects on the spin transport, have not been explicitly considered in the DFT-NEGF formalism. However, even if so, the main conclusion of nearly 100% spin polarization and giant TER and TMR will not be influenced, although they may have some quantitative effects. Moreover, compared with the factors such as the density of states, and spin matching and symmetry matching of wave functions, these will only be secondary effects in this study.

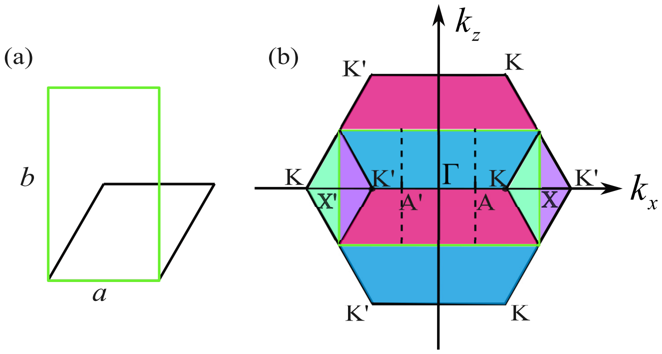

FIG. 7. The Brillouin-zone folding due to the supercell shape change with (a) the supercell from a rhombus to a rectangle, with $a = 7.62$ Å and $b = 13.20$ Å, and (b) the Brillouin-zone folding from a hexagon (black edge) to a rectangle (green edge). Due to the Brillouin-zone folding, the four blocks with different colors outside the rectangle will be moved into the rectangle to completely fill it after the vertical or horizontal shifting by a reciprocal lattice vector. The two vertical dashed lines indicate the region around the Γ point where there are no states.

Finally, we will understand the origin of the transmission gap around the Γ point in the $k_{//}$-resolved transmission function at the Fermi level, as shown in Fig. 6(d), from the band structure. Since the transmission in the junction is mediated by the VSi_2N_4 layer, we only need to focus on the projected spin-up band structure of VSi_2N_4 in Fig. 3(a), which is shown for the hexagon Brillouin zone of the rhombus supercell. It is found that the spin-up conduction band crosses the Fermi level around the K point. In the meantime, there are no states around the Γ point. After transforming from the rhombus supercell to the rectangle supercell taken in the transport calculations, the first Brillouin-zone shape is folded from a hexagon into a rectangle (Fig. 7). Since the transverse (transport) direction is along a (b) with the shorter (longer) lattice constant [Fig. 7(a)], all the K and K' points in the hexagon are folded onto the corresponding the K and K' points in the k_x axis (the transverse direction), as shown in Fig. 7(b). The k point where the spin-up band of VSi_2N_4 crosses the Fermi level along the $K - \Gamma$ segment in Fig. 3(a) is folded to the A and

A' points in Fig. 7(b). There are no states between A and A' around the Γ point, and thus the transmission in this region will be negligible, which is the origin of the transmission gap in Fig. 6(d).

IV. CONCLUSION

In summary, we determined the structural stability and electrical characteristics of the multiferroic heterostructure VSi_2N_4/In_2Te_3 based on first-principles calculations. The calculated results show that the spin-polarized electronic structure of VSi_2N_4 can be effectively modulated by inverting the ferroelectric polarization of In_2Te_3, leading to a transition from semiconductor to half metal. That is, when coupled to the $P_\downarrow$ In_2Te_3 state (the "−" side), the VSi_2N_4 monolayer maintains its semiconducting nature. In contrast, it becomes half metallic when in contact with the $P_\uparrow$ In_2Te_3 state (the "+" side), and its spin-up energy band crosses the Fermi energy level. Such phase transition can lead to significant changes in the electronic transport properties. We have designed an atomically thick MTJ with a multiferroic VSi_2N_4/In_2Te_3 heterojunction as the electrode, and the ferromagnetic semiconductor VSi_2N_4 as the tunneling barrier. The calculated transmission spectrum shows that in the $P_\uparrow$ state, under the parallel magnetization configuration, only spin-up electrons tunnel through the MTJ, indicating nearly 100% spin polarization, whereas under the antiparallel magnetization configuration, almost no electrons tunnel through the MTJ, which results in a $1.93 \times 10^{12}\%$ TMR ratio. In contrast, in the $P_\downarrow$ state, both spin channels are almost completely blocked, leading to $1.72 \times 10^{17}\%$ TER ratio accompanying the polarization reversal. However, it should be noted that these values are achieved with the equilibrium conductance in ideal theoretical models. Practically, due to the factors such as finite-temperature effects and intermixing at the interface, the nearly 100% spin polarization and the extremely high TMR and TER ratios may be diminished to a certain extent. Nevertheless, since all these values originate from the half-metal characteristics of the VSi_2N_4 in the $P_\uparrow$ state and the insulator–half-metal transition during the $P_\downarrow \rightleftharpoons P_\uparrow$ reversal, these values will still be very high so that very good performance in terms of high spin polarization and TMR/TER ratios will always be observable, even with the existence of these factors. Consequently, the findings suggest that MTJs based on the VSi_2N_4/In_2Te_3 heterojunction have great potential for applications in multifunctional spintronic devices.

ACKNOWLEDGMENTS

We gratefully acknowledge the support from the National Natural Science Foundation of China (Grants No. 12074230, No. 12474047, and No. 11974355), the Fund for Shanxi "1331 Project," and the Research Project Supported by Shanxi Scholarship Council of China.

---

[1] A. Ilyas, S. Xiang, M. Chen, M. Y. Khan, H. Bai, P. He, Y. Lu, and R. Deng, Nonvolatile electrical control of 2D $Cr_2Ge_2Te_6$ and intrinsic half metallicity in multiferroic heterostructures, Nanoscale **13**, 1069 (2021).

[2] K. S. Novoselov, A. K. Geim, S. V. Morozov, D. Jiang, Y. Zhang, S. V. Dubonos, I. V. Grigorieva, and A. A. Firsov, Electric field effect in atomically thin carbon films, Science **306**, 666 (2004).

[3] S. Chaudhuri, A. Bhattacharya, A. Das, G. Das, and B. Dev, Strain driven anomalous anisotropic enhancement in the thermoelectric performance of monolayer MoS_2, Appl. Surf. Sci. **626**, 157139 (2023).

[4] J. Jiang, L. Xu, C. Qiu, and L.-M. Peng, Ballistic two-dimensional InSe transistors, Nature (London) **616**, 470 (2023).

[5] F. Xia, H. Wang, D. Xiao, M. Dubey, and A. Ramasubramaniam, Two-dimensional material nanophotonics, Nat. Photon. **8**, 899 (2014).

[6] J.-J. He, J.-B. Dong, Y. Zhang, Q.-Y. Cao, L.-X. Liu, J.-Y. Gu, M. Hua, J.-R. Yuan, and X.-H. Yan, P_3S nanoribbons with bidirectional superior spin thermoelectric properties, Phys. E **165**, 116116 (2025).

[7] R. Jiao, Q. Wei, L. Zhang, Y. Xie, J. He, Y. Zhou, L. Shen, and J. Yuan, Enhancement and modulation of valley polarization in Janus CrSSe with internal and external electric fields, Phys. Chem. Chem. Phys. **26**, 13087 (2024).

[8] C. Tan, X. Cao, X.-J. Wu, Q. He, J. Yang, X. Zhang, J. Chen, W. Zhao, S. Han, G.-H. Nam, M. Sindoro, and H. Zhang, Recent advances in ultrathin two-dimensional nanomaterials, Chem. Rev. **117**, 6225 (2017).

[9] N. Miao, B. Xu, N. C. Bristowe, J. Zhou, and Z. Sun, Tunable magnetism and extraordinary sunlight absorbance in indium triphosphide monolayer, J. Am. Chem. Soc. **139**, 11125 (2017).

[10] Y. Wang, F. Li, Y. Li, and Z. Chen, Semi-metallic Be_5C_2 monolayer global minimum with quasi-planar pentacoordinate carbons and negative Poisson's ratio, Nat. Commun. **7**, 11488 (2016).

[11] C. Gong, L. Li, Z. Li, H. Ji, A. Stern, Y. Xia, T. Cao, W. Bao, C. Wang, Y. Wang, Z. Q. Qiu, R. J. Cava, S. G. Louie, J. Xia, and X. Zhang, Discovery of intrinsic ferromagnetism in two-dimensional van der Waals crystals, Nature (London) **546**, 265 (2017).

[12] B. Huang, G. Clark, E. Navarro-Moratalla, D. R. Klein, R. Cheng, K. L. Seyler, D. Zhong, E. Schmidgall, M. A. McGuire, D. H. Cobden, W. Yao, D. Xiao, P. Jarillo-Herrero, and X. Xu, Layer-dependent ferromagnetism in a van der Waals crystal down to the monolayer limit, Nature (London) **546**, 270 (2017).

[13] M. Bonilla, S. Kolekar, Y. Ma, H. C. Diaz, V. Kalappattil, R. Das, T. Eggers, H. R. Gutierrez, M.-H. Phan, and M. Batzill, Strong room-temperature ferromagnetism in VSe_2 monolayers on van der Waals substrates, Nat. Nanotechnol. **13**, 289 (2018).

[14] Y. Deng, Y. Yu, Y. Song, J. Zhang, N. Z. Wang, Z. Sun, Y. Yi, Y. Z. Wu, S. Wu, J. Zhu, J. Wang, X. H. Chen, and Y. Zhang, Gate-tunable room-temperature ferromagnetism in two-dimensional Fe_3GeTe_2, Nature (London) **563**, 94 (2018).

[15] N. Miao, B. Xu, L. Zhu, J. Zhou, and Z. Sun, 2D intrinsic ferromagnets from van der Waals antiferromagnets, J. Am. Chem. Soc. **140**, 2417 (2018).

[16] Q. Wu, Y. Zhang, Q. Zhou, J. Wang, and X. C. Zeng, Transition-metal dihydride monolayers: A new family of two-dimensional ferromagnetic materials with intrinsic room-temperature half-metallicity, J. Phys. Chem. Lett. **9**, 4260 (2018).

[17] C. Huang, Y. Du, H. Wu, H. Xiang, K. Deng, and E. Kan, Prediction of intrinsic ferromagnetic ferroelectricity in a transition-metal halide monolayer, Phys. Rev. Lett. **120**, 147601 (2018).

[18] D. J. O'Hara, T. Zhu, A. H. Trout, A. S. Ahmed, Y. K. Luo, C. H. Lee, M. R. Brenner, S. Rajan, J. A. Gupta, D. W. McComb, and R. K. Kawakami, Room temperature intrinsic ferromagnetism in epitaxial manganese selenide films in the monolayer limit, Nano Lett. **18**, 3125 (2018).

[19] C. Tan, J. Lee, S.-G. Jung, T. Park, S. Albarakati, J. Partridge, M. R. Field, D. G. McCulloch, L. Wang, and C. Lee, Hard magnetic properties in nanoflake van der Waals Fe_3GeTe_2, Nat. Commun. **9**, 1554 (2018).

[20] Q. Li, M. Yang, C. Gong, R. V. Chopdekar, A. T. N'Diaye, J. Turner, G. Chen, A. Scholl, P. Shafer, E. Arenholz, A. K. Schmid, S. Wang, K. Liu, N. Gao, A. S. Admasu, S.-W. Cheong, C. Hwang, J. Li, F. Wang, X. Zhang *et al.*, Patterning-induced ferromagnetism of Fe_3GeTe_2 van der Waals materials beyond room temperature, Nano Lett. **18**, 5974 (2018).

[21] A. V. Kuklin, S. A. Shostak, and A. A. Kuzubov, Two-dimensional lattices of VN: Emergence of ferromagnetism and half-metallicity on nanoscale, J. Phys. Chem. Lett. **9**, 1422 (2018).

[22] M. Ashton, D. Gluhovic, S. B. Sinnott, J. Guo, D. A. Stewart, and R. G. Hennig, Two-dimensional intrinsic half-metals with large spin gaps, Nano Lett. **17**, 5251 (2017).

[23] X. Zhou, X. Sun, Z. Zhang, and W. Guo, Ferromagnetism in a semiconducting Janus NbSe hydride monolayer, J. Mater. Chem. C **6**, 9675 (2018).

[24] Y. Guo, Y. Zhang, S. Yuan, B. Wang, and J. Wang, Chromium sulfide halide monolayers: Intrinsic ferromagnetic semiconductors with large spin polarization and high carrier mobility, Nanoscale **10**, 18036 (2018).

[25] P. Jiang, L. Kang, H. Hao, X. Zheng, Z. Zeng, and S. Sanvito, Ferroelectric control of electron half-metallicity in A -type antiferromagnets and its application to nonvolatile memory devices, Phys. Rev. B **102**, 245417 (2020).

[26] X. H. Zheng, X. L. Wang, T. A. Abtew, and Z. Zeng, Building half-metallicity in graphene nanoribbons by direct control over edge states occupation, J. Phys. Chem. C **114**, 4190 (2010).

[27] X. Zheng, X. Chen, L. Zhang, L. Xiao, S. Jia, Z. Zeng, and H. Guo, Perfect spin and valley polarized quantum transport in twisted SiC nanoribbons, 2D Mater. **4**, 025013 (2017).

[28] X. Tao, L. Zhang, X. Zheng, H. Hao, X. Wang, L. Song, Z. Zeng, and H. Guo, h-BN/graphene van der Waals vertical heterostructure: A fully spin-polarized photocurrent generator, Nanoscale **10**, 174 (2018).

[29] O. L. Sanchez, D. Ovchinnikov, S. Misra, A. Allain, and A. Kis, Valley polarization by spin injection in a light-emitting van der Waals heterojunction, Nano Lett. **16**, 5792 (2016).

[30] M. Wu, X. Wu, and X. C. Zeng, Exploration of half metallicity in edge-modified graphene nanoribbons, J. Phys. Chem. C **114**, 3937 (2010).

[31] E.-j. Kan, Z. Li, J. Yang, and J. G. Hou, Half-metallicity in edge-modified zigzag graphene nanoribbons, J. Am. Chem. Soc. **130**, 4224 (2008).

[32] P. Jiang, L. Kang, X. Zheng, Z. Zeng, and S. Sanvito, Computational prediction of a two-dimensional semiconductor with negative Poisson's ratio and tunable magnetism by doping, Phys. Rev. B **102**, 195408 (2020).

[33] Y.-W. Son, M. L. Cohen, and S. G. Louie, Half-metallic graphene nanoribbons, Nature (London) **444**, 347 (2006).

[34] C. Tang, L. Zhang, S. Sanvito, and A. Du, Electric-controlled half-metallicity in magnetic van der Waals heterobilayer, J. Mater. Chem. C **8**, 7034 (2020).

[35] J. Yu and W. Guo, A New paradigm to half-metallicity in graphene nanoribbons, J. Phys. Chem. Lett. **4**, 951 (2013).

[36] Q. Cui, Y. Zhu, J. Liang, P. Cui, and H. Yang, Spin-valley coupling in a two-dimensional VSi_2N_4 monolayer, Phys. Rev. B **103**, 085421 (2021).

[37] X. Wang, C. Zhu, Y. Deng, R. Duan, J. Chen, Q. Zeng, J. Zhou, Q. Fu, L. You, S. Liu, J. H. Edgar, P. Yu, and Z. Liu, Van der Waals engineering of ferroelectric heterostructures for long-retention memory, Nat. Commun. **12**, 1109 (2021).

[38] M. R. K. Akanda and R. K. Lake, Magnetic properties of $NbSi_2N_4$, VSi_2N_4, and VSi_2P_4 monolayers, Appl. Phys. Lett. **119**, 052402 (2021).

[39] X. Zhang, B. Liu, J. Huang, X. Cao, Y. Zhang, and Z.-X. Guo, Nonvolatile spin field effect transistor based on VSi_2N_4/Sc_2CO_2 multiferroic heterostructure, Phys. Rev. B **109**, 205105 (2024).

[40] S. Gao, F. Wei, B. Jia, C. Chen, G. Wu, J. Hao, W. Chen, L. Wu, W. Zou, and P. Lu, Two-dimensional van der Waals layered VSi_2N_4 as anode materials for alkali metal (Li, Na and K) ion batteries, J. Phys. Chem. Solids **178**, 111339 (2023).

[41] F. Wei, S. Gao, B. Jia, J. Hao, C. Chen, E. Abduryim, S. Guo, L. Gao, and P. Lu, First-principles computational study of Janus van der Waals layered $VSiGeN_4$ as anode material for Li-ion battery, Colloids Surf., A **681**, 132777 (2024).

[42] J. Chen and Q. Tang, The versatile electronic, magnetic and photo-electro catalytic activity of a new 2D MA_2Z_4 family, Chem. A: Eur. J. **27**, 9925 (2021).

[43] G. Kresse and J. Furthmüller, Efficient iterative schemes for *ab initio* total-energy calculations using a plane-wave basis set, Phys. Rev. B **54**, 11169 (1996).

[44] G. Kresse and D. Joubert, From ultrasoft pseudopotentials to the projector augmented-wave method, Phys. Rev. B **59**, 1758 (1999).

[45] P. E. Blöchl, Projector augmented-wave method, Phys. Rev. B **50**, 17953 (1994).

[46] J. P. Perdew, K. Burke, and M. Ernzerhof, Generalized gradient approximation made simple, Phys. Rev. Lett. **77**, 3865 (1996).

[47] S. Grimme, Semiempirical GGA-type density functional constructed with a long-range dispersion correction, J. Comput. Chem. **27**, 1787 (2006).

[48] L. Bengtsson, Dipole correction for surface supercell calculations, Phys. Rev. B **59**, 12301 (1999).

[49] Y. Feng, J. Han, K. Zhang, X. Lin, G. Gao, Q. Yang, and S. Meng, van der Waals multiferroic tunnel junctions based on sliding multiferroic layered, Phys. Rev. B **109**, 085433 (2024).

[50] S. Smidstrup, T. Markussen, P. Vancraeyveld, J. Wellendorff, J. Schneider, T. Gunst, B. Verstichel, D. Stradi, P. A. Khomyakov, U. G. Vej-Hansen, M.-E. Lee, S. T. Chill, F. Rasmussen, G.

Penazzi, F. Corsetti, A. Ojanperä, K. Jensen, M. L. N. Palsgaard, U. Martinez, A. Blom *et al.*, QuantumATK: an integrated platform of electronic and atomic-scale modelling tools, J. Phys.: Condens. Matter **32**, 015901 (2020).

[51] J. Taylor, H. Guo, and J. Wang, *Ab initio* modeling of quantum transport properties of molecular electronic devices, Phys. Rev. B **63**, 245407 (2001).

[52] Y.-L. Hong, Z. Liu, L. Wang, T. Zhou, W. Ma, C. Xu, S. Feng, L. Chen, M.-L. Chen, D.-M. Sun, X.-Q. Chen, H.-M. Cheng, and W. Ren, Chemical vapor deposition of layered two-dimensional $MoSi_2N_4$ materials, Science **369**, 670 (2020).

[53] Z. Wang, M. Safdar, C. Jiang, and J. He, High-performance UV–visible–NIR broad spectral photodetectors based on one-dimensional In_2Te_3 nanostructures, Nano Lett. **12**, 4715 (2012).

[54] L. Wang, Y. Shi, M. Liu, A. Zhang, Y.-L. Hong, R. Li, Q. Gao, M. Chen, W. Ren, H.-M. Cheng, Y. Li, and X.-Q. Chen, Intercalated architecture of MA_2Z_4 family layered van der Waals materials with emerging topological, magnetic and superconducting properties, Nat. Commun. **12**, 2361 (2021).

[55] A. Kahn, Fermi level, work function and vacuum level, Mater. Horiz. **3**, 7 (2016).

[56] J. Kang, W. Liu, D. Sarkar, D. Jena, and K. Banerjee, Computational study of metal contacts to monolayer transition-metal dichalcogenide semiconductors, Phys. Rev. X **4**, 031005 (2014).

[57] A. Xie, H. Hao, C.-S. Liu, X. Zheng, L. Zhang, and Z. Zeng, Giant tunnel electroresistance in two-dimensional ferroelectric tunnel junctions constructed with a van der Waals ferroelectric heterostructure, Phys. Rev. B **107**, 115427 (2023).

[58] L. Kang, P. Jiang, H. Hao, Y. Zhou, X. Zheng, L. Zhang, and Z. Zeng, Giant tunnel electroresistance in ferroelectric tunnel junctions with metal contacts to two-dimensional ferroelectric materials, Phys. Rev. B **103**, 125414 (2021).

[59] L. Kang, P. Jiang, H. Hao, Y. Zhou, X. Zheng, L. Zhang, and Z. Zeng, Giant tunneling electroresistance in two-dimensional ferroelectric tunnel junctions with out-of-plane ferroelectric polarization, Phys. Rev. B **101**, 014105 (2020).

[60] Q. Wu, L. Shen, M. Yang, J. Zhou, J. Chen, and Y. P. Feng, Giant tunneling electroresistance induced by ferroelectrically switchable two-dimensional electron gas at nonpolar $BaTiO_3/SrTiO_3$ interface, Phys. Rev. B **94**, 155420 (2016).

[61] M. Li, L. L. Tao, and E. Y. Tsymbal, Domain-wall tunneling electroresistance effect, Phys. Rev. Lett. **123**, 266602 (2019).